

---

# Amplitude Distributions of Dark Counts and Photon Counts in NbN Superconducting Single-Photon Detectors Integrated with a High-Electron Mobility Transistor Readout

## Introduction

Fast and reliable single-photon detectors (SPD's) have become a highly sought after technology in recent years.<sup>1</sup> Some of the most-interesting applications for SPD's, which include quantum communications and quantum key distribution<sup>2</sup> as well as satellite communications, require devices that can successfully operate at telecommunication wavelengths, namely 1310 nm and 1550 nm. Additional very desirable features for ideal SPD's are their photon-number resolution (PNR) capability,<sup>3,4</sup> e.g., for all-optical quantum computing, and their photon-energy sensitivity (PES),<sup>5</sup> e.g., for spectral observations of so-called photon-starved objects. InGaAs avalanche photodiodes work at telecommunication wavelengths and are commercially available; they do, however, suffer from severe after-pulsing and require time gating, which limits their maximum count rate. Presently, they also lack advanced PNR and PES capabilities.<sup>6,7</sup>

It has already been established that nanostructured, NbN superconducting SPD's (SSPD's) operate based on hot-spot formation and bias-current redistribution in ultrathin (4-nm), ultranarrow (100- to 120-nm), and long (~0.5-mm) meandering NbN superconductive nanostripes.<sup>1,8</sup> NbN SSPD's have been shown to have counting rates exceeding 250 MHz, with reported quantum efficiencies (QE's) up to 57% (Ref. 9) at 1550-nm wavelength and very low, <10-Hz to 10-kHz dark-count rates, depending on the operation bias point.<sup>10</sup>

Typically, the SSPD's are kept at temperatures between 1.7 and 4.2 K (far below the NbN critical temperature  $T_c$ ) and biased at currents  $I_{\text{bias}}$  close to the meandering stripe critical current  $I_c$ . Once a photon is absorbed by the NbN nanostripe, it breaks a Cooper pair, and, subsequently, a large number of quasiparticles are generated through the electron–electron and electron–phonon interactions, creating a local hot spot, where superconductivity is suppressed or even destroyed. The hot spot expels the supercurrent from its volume and forces it to flow near the stripe edges, where it can exceed the  $I_c$  value, leading to the generation of phase-slip centers and the eventual formation of a resistive region (joule heating) across the width of the stripe.

When the SSPD device is directly connected to a transmission line with a characteristic impedance  $Z_0$  equal to, e.g., 50  $\Omega$ , the above-mentioned resistive region, which is typically  $\gg 50 \Omega$ , forces the bias current to redistribute from the SSPD into the load, which means that the amplitude of the SSPD voltage response is always measured across the constant  $Z_0$ . The above conclusion would be true even if the SSPD were simultaneously illuminated by several photons and, consequently, several hot spots were simultaneously generated at various points along the meander. Therefore, in the above experimental arrangement, which is actually typical for the vast majority of published work, the SSPD photoresponse is insensitive to both the number and energy of incoming photons, and the device acts as a simple photon-event counter rather than an energy and/or spectrally sensitive detector.

We need to stress here that a biased SSPD can generate output electrical pulses even when the input light is completely blocked and there are no photons incident on the device. Those so-called dark-count pulses are transient voltage signals, spontaneously generated in a long, current-biased, superconducting nanostripe, and, when the device is connected to an output of a coaxial line, their amplitude is limited by  $Z_0$  despite the fact that the physical origin of dark counts is different from that responsible for photon counts. In the case of dark counts, the transient resistive state across the SSPD nanostripe is actually caused by the current-induced generation and propagation of free vortex–antivortex pairs.<sup>11,12</sup> Therefore, in experimental studies of the SSPD performance, it would be very important to be able to distinguish the photon counts from the dark counts.

The goal of this work is to show that, with our recently developed new readout scheme that implements a low-noise, cryogenic, high-electron-mobility transistor (HEMT) and a high-load resistor next to the detector,<sup>13</sup> we are able, albeit not in real time, to resolve the difference between the SSPD dark- and photon-count events by collecting histograms of the output-pulse distributions and, subsequently, comparing their mean amplitudes and distribution widths. We also present our early findings that demonstrate that the same readout approach

can lead to some PNR functionality in SSPD's, as predicted in Ref. 14. We stress that although the research presented here is rather preliminary, it does represent an important step toward making SPD's true photon sensor-type devices with energy resolution.

This article begins with a brief description of the SSPD fabrication process and presents our experimental setup based on the high-input-impedance HEMT readout circuit. Next, we introduce a simple equivalent circuit of the SSPD, based on the fixed-equivalent-resistance hot-spot model and discuss its practical limitations, namely, the conditions that are needed to fulfill the requirement that the readout input impedance is always the dominant factor. Our experimental data are, subsequently, presented and consist of long, real-time SSPD traces collected either under photon illumination or in the dark. A statistical approach is used for the data analysis to calculate the corresponding distributions functions. The comparison between the distributions' mean amplitudes and widths enables one to quantitatively distinguish photon absorption events from dark counts. The presented analysis demonstrates how experimental data collected by an SSPD directly connected to the high-impedance readout can either shed light on the average photon number of the incident ultraweak flux of monochromatic light or provide some spectral characterization of multicolor pulses. Finally, a summary and concluding remarks are presented.

### Device Description and Experimental Setup

SSPD's were patterned from epitaxial-quality NbN films, deposited by dc reactive magnetron sputtering onto sapphire substrates.<sup>15</sup> The films were characterized by a sheet resistance between 400 and 500  $\Omega/\text{sq}$  at room temperature, with  $T_c$  between 10 and 11 K, and the critical current density  $J_c \approx 10^6$  A/cm<sup>2</sup>. The meander patterning was done by e-beam lithography and reactive-ion etching. It is important to note here that while the films were deposited at the Moscow State Pedagogical University, they were patterned at Delft University of Technology. Apparently, slight differences in geometry or in the patterning method were responsible for the fact that the SSPD's in this work had 3 $\times$ - to 4 $\times$ -lower  $I_c$ 's ( $\sim 5$  to 10  $\mu\text{A}$ ) than the typical Moscow devices.<sup>15</sup> The QE's, however, were on a par with the standard  $10 \times 10\text{-}\mu\text{m}^2$  SSPD's, with the devices measured in this work having  $\text{QE} \approx 3\%$  to  $5\%$  at  $\lambda = 800$  nm.

The standard SSPD operation setup is shown in Fig. 129.46(a). The device was wire bonded to a 50- $\Omega$  microstrip transmission line, coupled to a multimode optical fiber, and immersed in liquid helium.<sup>16</sup> The microstrip was then connected to a semi-rigid coaxial cable and, at room temperature, connected to a

custom-made, wideband bias-tee (0.08- to 26-GHz bandwidth). The bias-tee enabled us to simultaneously amplify the transient photoresponse signal using a tandem of two broadband amplifiers (0.08- to 8.5-GHz bandwidth, 22-dB gain) and to dc bias both the SSPD and HEMT. The amplified output signals, corresponding to photon counts and/or dark counts, were recorded by using either a Tektronix digital single-shot oscilloscope (6-GHz bandwidth) or a pulse counter. As a photon source, we used a train of 100-fs-wide, 800-nm-wavelength pulses, generated by a mode-locked Ti:sapphire laser at a rate of 82 MHz. The pulses were heavily attenuated to precisely control the average number of photons per pulse. For dark-count measurements, the detector was blocked from all incoming radiation, i.e., shielded inside the Dewar by a metallic enclosure.

An equivalent electrical model of the SSPD photoresponse is shown in Fig. 129.46(b). Kinetic inductance  $L_k$  is in series with a parallel arrangement of a hot-spot resistance  $R_{\text{hs}}$ , and a switch  $S$  represents the photodetection (switching) event in the SSPD.<sup>17</sup> The detector is then connected to a dc bias source and a readout circuit, which, in this case, consists of a transmission line with input impedance  $Z_0 = 50 \Omega$ . In the simulations presented on p. 41, we also took into account [not shown in Fig. 129.46(b)] a small, parasitic on-board capacitance and a bandpass filter representing the bandwidth of an outside (room-temperature) amplifier. Finally,  $V_{\text{out}}$  is the experimentally observed transient voltage pulse during photodetection.

Initially, the switch is closed and there is no voltage drop. Once a photon is absorbed by our nanostripe, the switch opens, and as  $R_{\text{hs}}$  grows to a value much larger than  $Z_0$ , most of the

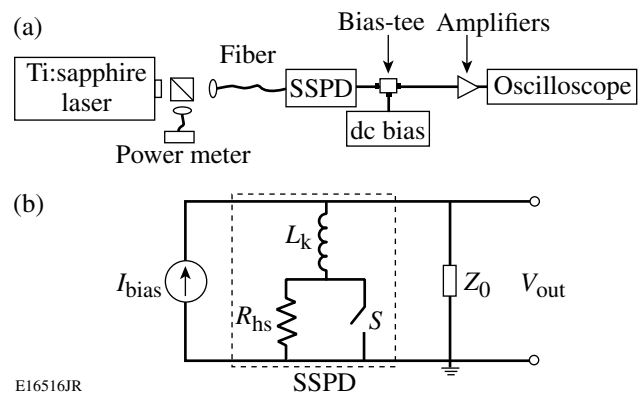


Figure 129.46

(a) Experimental setup and (b) standard electrical photoresponse model of SSPD (superconducting single-photon detector).

current redistributes into  $Z_0$ , and the resultant voltage pulse amplitude is simply  $V_{out} \approx Z_0(I_{bias} - I_{ret})$ , where  $I_{ret}$  is the value of current flowing through the device at the highest value of  $R_{hs}$  (Ref. 17). Therefore, independent of the number or energy of the absorbed incident photons,  $V_{out}$  always has the same value for a given  $I_{bias}$  for the circuit shown in Fig. 129.46(b).

Our high-impedance readout scheme, presented in Fig. 129.47, was first described in Ref. 13 and, as already outlined there, it implements a commercial HEMT, operated cryogenically, and mounted next to (on the same board) the SSPD. The HEMT acts as an infinite-impedance element to separate the 50-Ω output transmission line from the SSPD. Because the HEMT input impedance is very high, a 500-Ω load (or shunt) resistor  $R_L$  is also used in parallel with the detector and the HEMT, as shown in Fig. 129.47. As mentioned previously, both the SSPD and HEMT were biased through the same custom-made, wideband bias-tee. Such an integrated arrangement enables one to bias the devices using  $R_{bias} = 150$  kΩ, mounted on the board together with the rest of the components and, simultaneously, to read out the ac photoresponse voltage signal.

By applying the detector transient response to the gate of the HEMT, one can read out the drain voltage, which should, ideally (for  $R_L \gg R_{hs}$ ), be proportional to the hot-spot resistance and equal to  $V_{out}$ . If the number of photons simultaneously absorbed in the SSPD meander happens to be larger than 1, the photons are likely to form separate hot spots and their resistances will add up in series. The HEMT output voltage in this simplest case should be  $V_{out} \approx (I_{bias} - I_{ret})nR_{hs}$ , where  $n$  is the number of absorbed photons per pulse (actually, the number of created hot spots). Therefore, for relatively small  $n$ 's,

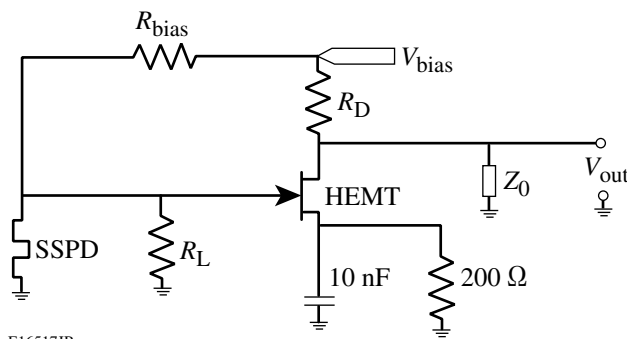


Figure 129.47  
Circuit schematics implementing a HEMT (high-electron-mobility transistor) amplifier and 500-Ω load resistor  $R_L$ . The 10-nF capacitor sets the maximum ac gain and the 200-Ω resistor sets the dc current for the HEMT;  $R_{bias}$  and  $R_D$  are the biasing and pull-up resistors, respectively.

and in the case of  $nR_{hs} < R_L$ , the output-pulse height of our setup is proportional to  $n$ , effectively leading to PNR, as was theoretically discussed and modeled in Ref. 14.

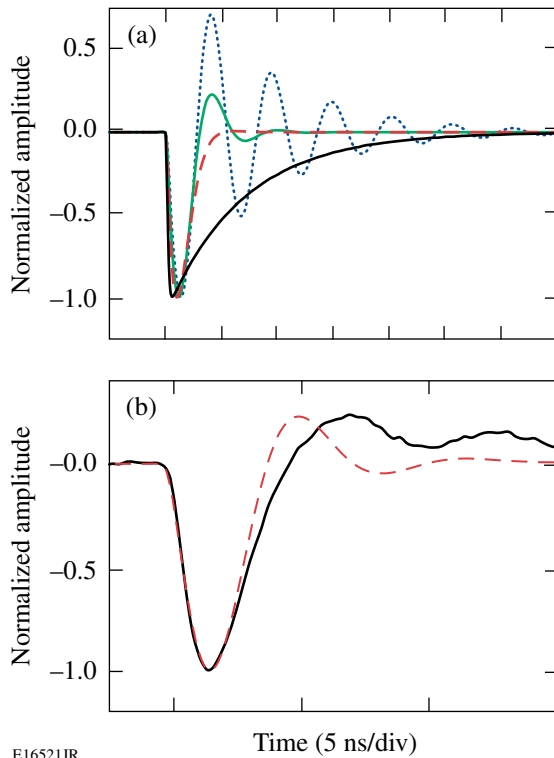
Based on an intrinsic difference in the physics mechanisms of the generation of photon and dark-count transients in SSPD's discussed above, the HEMT setup should also enable one to distinguish pulses generated in response to either a single-photon absorption event (photon count) or a spontaneous voltage transient (dark count). In the case of dark counts, one can expect only a single localized resistive region, created by the vortex-antivortex pair's (VAP's) motion across the stripe,<sup>12</sup> with the effective resistance different than  $R_{hs}$ , resulting in a somewhat different value of  $V_{out}$ . In the full analogy, it is expected that photons of different energies should produce hot spots with different  $R_{hs}$  values, so our SSPD with the HEMT readout should possess PES functionality.

### Readout Circuit Simulations and Model Limitations

Our HEMT approach takes advantage of the simple fact that the greater the  $R_L$ , the more sensitive the readout in terms of either PNR or PES. Unfortunately, this cannot be easily accomplished since the large  $R_L$  values lead to an underdamped circuit behavior (see Fig. 129.48) because of a very large value of the indicator ( $L_k \sim 400$  nH) of our SSPD<sup>17</sup> in parallel with  $R_L$ . Figure 129.48(a) shows the PSpice<sup>a</sup>-simulated pulses for different values of  $R_L$ . Critical damping yields  $R_L = 270$  Ω (red curve) in Fig. 129.48(a), and it can be seen that for  $R_L = 500$  Ω (green curve), the circuit is already slightly underdamped since a small, damped oscillation follows the main pulse. Figure 129.48(b) shows an experimental voltage pulse (black line) obtained using our HEMT readout approach, as well as a simulated one (red dashed line). The slow, damped oscillations behind the measured main pulse are caused by some second-order, capacitive effects from the HEMT circuit and/or stainless-steel coaxial line. An associated small parasitic capacitance (not shown in Fig. 129.47) has been estimated to be 2 to 3 pF, by looking at the oscillation frequency of the underdamped pulse.

Our tested SSPD's typically exhibited  $I_c \approx 5$  μA, leading to the roughly estimated  $R_{hs}$  value to be between 600 and 1000 Ω. Therefore, based on the behavior observed in Fig. 129.48, we selected  $R_L = 500$  Ω for all our experiments as a compromise between the optimal value (minimal oscillations) from the

<sup>a</sup>PSpice (currently available from OrCAD Corp. of Cadence Design Systems) is a PC version of SPICE, originally developed at the Electronics Research Laboratory of the University of California, Berkeley (1975).



E16521JR

Figure 129.48

(a) PSpice simulations of voltage transients at different values of  $R_L$ :  $50\ \Omega$  (black curve),  $270\ \Omega$  (red dashed curve),  $500\ \Omega$  (green curve), and  $2\ \text{k}\Omega$  (blue dotted curve); (b) measured photoresponse (black curve) and simulated photoresponse (red dashed curve) for  $R_L = 500\ \Omega$ .

circuit point of view and the need to have  $R_L$  as large as possible to achieve PNR functionality. Since  $R_L = 500\ \Omega$  is at best comparable to  $R_{\text{hs}}$ , the experimentally measured  $V_{\text{out}}$  readout signal amplitude is proportional to a parallel connection of  $R_L$  and  $R_{\text{hs}}$ , limiting the ability to fully quantitatively distinguish between the different types of SSPD counting events. Therefore, the experimental observations presented here are mainly qualitative. In addition, since real-time analysis has been inconclusive, it was decided to use a statistical approach to analyze our experimental data.

Our approach of an SSPD integrated with an HEMT readout with a fixed  $R_L = 500\ \Omega$  value can work satisfactorily, as will be shown later, but only for devices with rather small  $I_c$  and, consequently, typically, low QE. In large-QE SSPD's biased close to  $I_c$ , as shown in Ref. 18, the  $R_{\text{hs}}$  can be as large as  $5.5\ \text{k}\Omega$ , mainly because of joule heating. Joule heating of the nanostripe turns it completely resistive and occurs in parallel with the hot-spot cooling process and current redistribution.<sup>18</sup> The latter can be well illustrated looking at the time-domain evolution of the photoresponse transient. Based on the electri-

cal model shown in Fig. 129.47, the difference in amplitude for different hot-spot resistances stem from variations in the time interval it takes for the current initially biasing the device to redistribute into the readout circuit. In other words, for a given  $R_L$ , current redistribution time decreases with increasing  $R_{\text{hs}}$ . For the hot spot to stop growing and the cooling mechanism to take over, the current through the device must drop to a value below approximately 20% of  $I_c$  (Ref. 19). When the SSPD photoresponse is modeled such that  $R_{\text{hs}}$  is a simple resistor, the fall and rise time constants of the transient  $V_{\text{out}}$  are simply  $\tau_{\text{fall}} = L_k / (R_{\text{hs}} + R_L)$  and  $\tau_{\text{rise}} = L_k / R_L$  (Ref. 17), respectively. On the other hand, if  $R_{\text{hs}}$  progressively increases during the current redistribution, the entire process becomes nonlinear and the transient decay cannot be modeled by a simple exponential function. From the readout circuit point of view, this is a very challenging problem since even if it were possible to find a cryogenic amplifier with large enough  $R_L$ , the readout scheme would not work because the current would not be able to redistribute into the load fast enough to prevent a runaway heating effect that would cause the device to simply latch.

We believe the best approach to restrict the uncontrolled growth of  $R_{\text{hs}}$  and, consequently, suppress the heat runaway effect is to significantly improve the heat transport between the superconductor and the substrate (single-crystal sapphire for “standard” SSPD's), either by using substrates, which are a better acoustic-phonon match to NbN, or by changing the nanostripe material. In the latter case, the ferromagnet/superconductor nanostructured bilayers are very promising because, as has recently been shown, they exhibit much-faster electron-phonon dynamics, as compared to plain Nb or NbN.<sup>20,21</sup>

## Results and Discussion

During the course of our experiments, we have collected very long (millions of pulses) real-time traces by continuously recording either photon-count events or dark counts. In the latter case, the voltage response was measured when an SSPD was completely isolated from the outside world. Figures 129.49(a) and 129.49(b) present randomly selected, short sections of photon-count traces of output pulses (after amplification) recorded in time-domain when an SSPD was connected either according to the conventional  $50\text{-}\Omega$  scheme [Fig. 129.46(b)] or a scheme with an HEMT readout (Fig. 129.47), respectively. The incident laser intensity was adjusted in such a way that nearly every photon pulse was registered by the detector (for an SSPD with  $\text{QE} \approx 5\%$  that corresponds to  $\sim 500$  photons per pulse). These plots are intended to illustrate a qualitative difference in the recorded photoresponse signals, since even from such short “snapshots,” it can clearly be seen that while in the

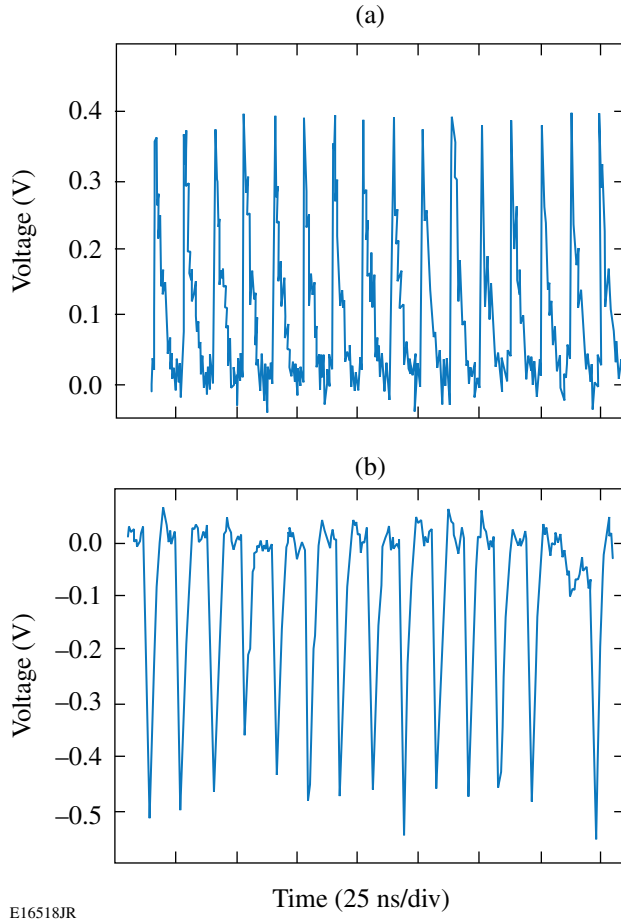


Figure 129.49

Comparison of live oscilloscope time-domain traces for (a) a traditional scheme and (b) an HEMT readout scheme, taken at similar laser intensities, such that  $n \leq 1$  (HEMT is an inverting amplifier; therefore the pulses are negative). Here,  $n$  is the number of absorbed photons per pulse. The laser repetition rate is 82 MHz.

case of the conventional biasing technique, pulse amplitudes remain essentially constant, the HEMT readout allows one to record at least some quantitative differences between the different SSPD counting events.

For a more-quantitative analysis, a statistical approach was used to compute the distribution functions of amplitudes of pulses recorded under different experimental conditions. Figure 129.50 shows histograms that compare pulse-amplitude distributions of dark counts [Fig. 129.50(a)], as well as the photon counts collected at two different laser intensities [Figs. 129.50(b) and 129.50(c)]. All data were taken using the HEMT readout and in each case the SSPD was biased using  $I_{\text{bias}} = 0.9 I_c$ . All histograms were fitted with a simple Gaussian function and it is clear that the dark counts [Fig. 129.50(a)]

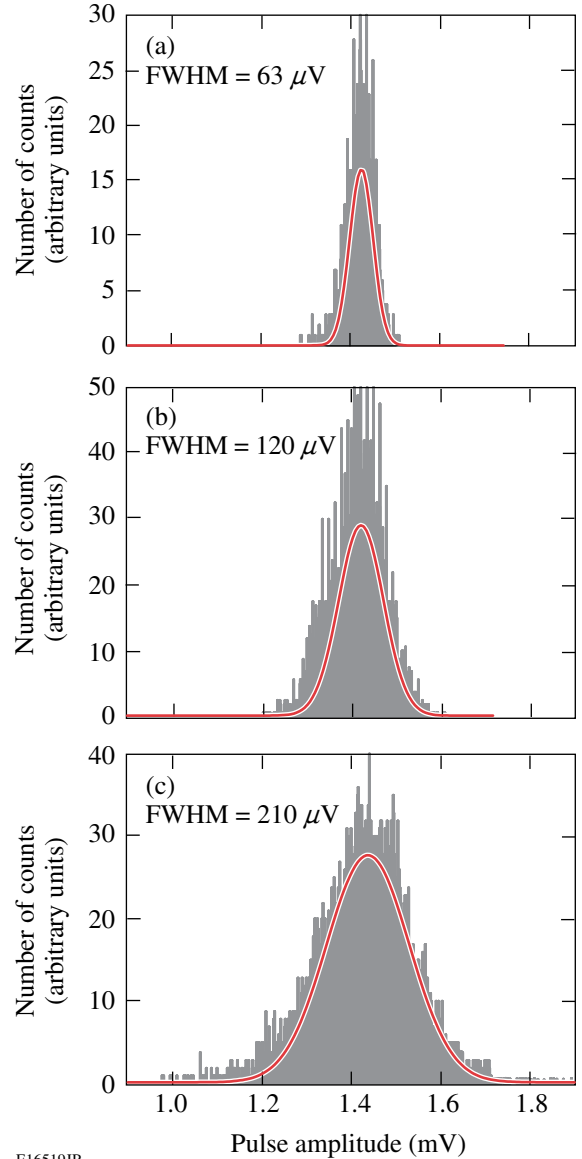


Figure 129.50

(a) Pulse-amplitude histograms of dark counts, (b) photon counts in the single-photon regime  $n \sim 1$ , and (c) multiphoton regime  $n \geq 1$ . All measurements performed the HEMT readout at 4.2 K and at  $I_{\text{bias}} = 0.9 I_c$ . The SSPD output-voltage amplitudes are divided by the amplifier gain.

exhibit the narrowest full-width-at-half-maximum (FWHM) distribution. For the photon counts, we observe a widening of the Gaussian distribution as we move from the single-photon regime [ $n \sim 1$ ; Fig. 129.50(b)] to the multiphoton case [ $n \geq 1$ ; Fig. 129.50(c)]. In principle, the observed increase in the width of the Gaussian distribution for the photon counts could have resulted from excess shot noise. To verify this hypothesis, we have additionally recorded a histogram (Fig. 129.51) of output pulses collected when the SSPD was operated under the same

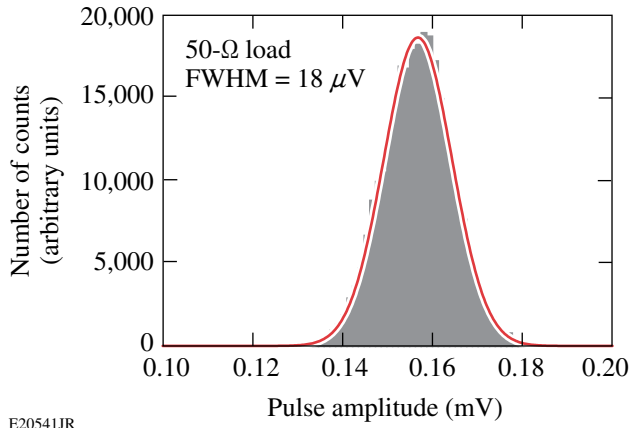
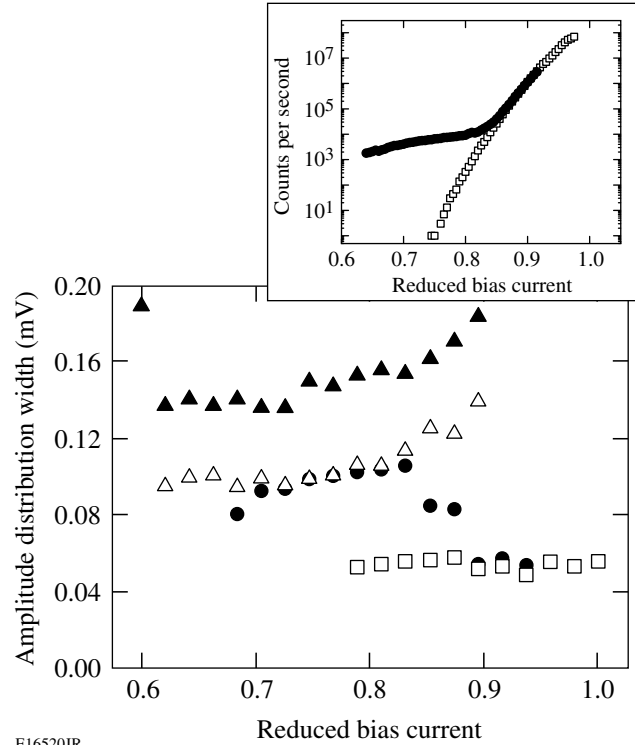


Figure 129.51

Pulse-amplitude histogram of photon counts in the single-photon regime ( $n \sim 1$ ), when the SSPD was directly connected to the 50- $\Omega$  output coaxial line (no HEMT readout). All measurements were performed at 4.2 K and  $I_{\text{bias}} = 0.9 I_c$ . The SSPD output-voltage amplitudes are divided by the amplifier gain.

conditions as in Fig. 129.50(b), namely, in the single-photon regime; however, in that case, our detector was directly connected to the 50- $\Omega$  output line. We note that the histogram shown in Fig. 129.51 exhibits almost a perfect Gaussian distribution with a very narrow, noise-delimited width. Therefore, the impact of the shot noise is negligible and we can conclude that, indeed, the HEMT readout allows one to get at least a quantitative insight on the amplitude variations of the SSPD voltage output pulses, when the device is operated under different experimental conditions, e.g., the different incident photon flux levels.

A large number of histograms of the type presented in Fig. 129.50 have been collected under different SSPD biasing and optical illumination conditions. The correlation between the photon flux (average number of photons per pulse) incident upon the detector and the FWHM of the resulting distribution of the response pulse amplitudes was very reproducible and is summarized in Fig. 129.52, where the FWHM of the signal amplitude histograms versus the SSPD normalized current bias  $I_{\text{bias}}/I_c$  is presented, for both the dark counts (open squares) and the photon counts corresponding to the multiphoton ( $n \geq 1$ , closed triangles), single-photon ( $n \sim 1$ ; open triangles), and heavily attenuated ( $n \ll 1$ ; closed circles) illumination. We see that the dark-count signals exhibit the narrowest FWHM, which, in addition, is independent of the bias. Substantial differences also exist between the FWHM values corresponding to different incident photon fluxes. The general trend is that the distribution width increases with increasing  $I_{\text{bias}}/I_c$ , which is caused by the increased SSPD sensitivity in the  $I_{\text{bias}} \approx I_c$



E16520JR

Figure 129.52

Amplitude distribution width (FWHM of Gaussian fits) for dark counts (open squares),  $n < 1$  (closed circles),  $n \sim 1$  (open triangles), and  $n \geq 1$  (closed triangles). The inset shows the counting rate as a function of bias current for dark counts (open squares) and  $n < 1$  (closed circles).

biasing regime, where even photons hitting the edges of the nanostripe are likely to be counted.<sup>22</sup> On the other hand, for a very low photon flux ( $n \ll 1$ ; closed circles in Fig. 129.52), the amplitude distribution FWHM starts to drop around  $I_{\text{bias}} = 0.83 I_c$ , eventually overlapping (open squares) at  $I_{\text{bias}} > 0.9 I_c$ , as the dark counts dominate over the photon counts. The latter behavior agrees very well with our earlier observation<sup>11</sup> of the near-exponential dependence of the rate of dark counts in SSPDs on the  $I_{\text{bias}}/I_c$  ratio and their dominance in the  $I_{\text{bias}} \approx I_c$  limit, as shown in the inset in Fig. 129.52.

The significant difference (a factor of several) in the FWHM values of the histograms for the dark- and photon-count events collected for the SSPD with the HEMT readout must have come from the intrinsic difference in the physics of triggering those counts. As demonstrated in Ref. 12, when a current-biased SSPD is blocked from all incoming radiation (shielded by a metallic enclosure) and placed in liquid helium, the spontaneous transient voltage pulses, or dark counts, are primarily caused by topological excitations. The thickness of the NbN stripe is 4 nm and the width is  $\sim 100$  nm, which puts

the SSPD nanostripe in a two-dimensional (2-D) superconductor regime because its thickness is smaller, but the width is much larger than the NbN Ginsburg–Landau coherence length ( $\sim 6$  nm at  $T = 0$  K). In 2-D systems in general, true long-range superconducting order is not possible, and in an ultrathin film, topological excitations come in the form of VAP's.<sup>23</sup> At typical SSPD operating temperatures far below  $T_c$  and in the absence of  $I_{\text{bias}}$ , all VAP's are bound and there is no dissipation in the NbN stripe. Once  $I_{\text{bias}}$  is applied, it exerts a Lorentz force on the VAP's, and at  $I_{\text{bias}}$  close to  $I_c$ , this force is strong enough to exceed the VAP binding energy and to break them. The latter effect creates free vortices and antivortices—analogue to excited electrons and holes in semiconductors—and allows them to move in opposite directions toward the edges of the NbN stripe, causing dissipation and resulting in the resistive state.<sup>24</sup> Since the VAP breaking events originate exclusively at the “weakest” (narrowest and/or localized) constriction spots of the SSPD meander, the normal region produced from these events is going to have only minimal variations in the resistance and, consequently, the histogram of the corresponding voltage pulses is expected to exhibit a very narrow distribution.

The fact that the photon-count amplitude distributions have FWHM's consistently wider than those corresponding to the dark counts (even in the single-photon regime) can be well understood based on the hot-spot–driven photon-detection events. Photon absorption and resulting hot-spot formation can happen at any point along the meander, leading to natural variations in the size of the resistive state.<sup>22</sup> Since the device  $I_c$  is determined by the narrowest and thinnest section(s) of the stripe, fabrication-related fluctuations in the stripe's cross section (variations in the width and/or thickness of the NbN stripe very likely to occur in our relatively low-QE SSPD's) must lead to the  $R_{\text{hs}}$  variations, which, in the case of our HEMT readout scheme, will be detected as the amplitude spread of photon-count responses. Finally, when the light intensity is relatively high ( $n \geq 1$ ), multiphoton-absorption events are likely to happen, especially for  $I_{\text{bias}}$  approaching  $I_c$ , as more sections of the SSPD meander are activated. As a result, we should observe enhanced fluctuations in the response pulse amplitudes and, correspondingly, to the widest distribution FWHM, as, indeed, is presented in Figs. 129.50(c) and 129.52.

### Toward Photon-Number Resolution

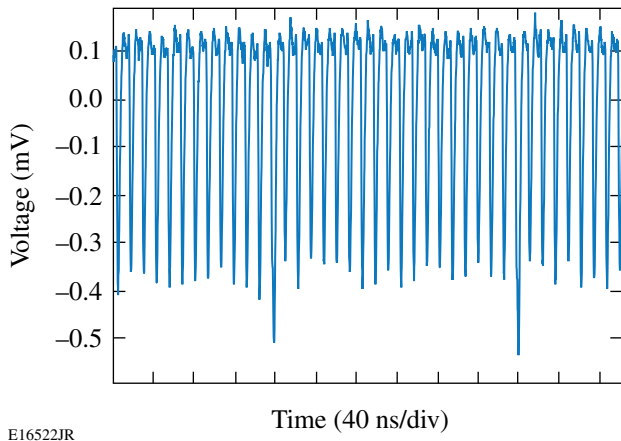
As mentioned before and predicted in Ref. 14, the integrated, cryogenic HEMT readout should not only allow one to distinguish dark counts from photon counts but also enable one to achieve PES and PNR in SSPD's. According to Ref. 14, a clear, real-time resolution between, e.g., the single- and two- or

three-photon events, requires  $R_L \gg R_{\text{hs}}$ . Since in our HEMT readout  $R_L$  is fixed and equal to  $500 \Omega$ , the latter condition is not fulfilled in our experiments, as already discussed in **Device Description and Experimental Setup**, p. 40, and we have to restrict ourselves to the statistical, post-processing analysis. Such an approach is obviously not practical for, e.g., optical quantum computing but can find extended applications in spectral characterization of unknown ultraweak light sources in astronomical observations.

We have already successfully implemented the statistical approach to demonstrating the SSPD PES capability in conventionally biased devices, where, by measuring the SSPD system's detection efficiency at different bias currents, we were able to resolve the wavelength of the incident photons with a resolution of 50 nm (Ref. 5). Using the statistical method, we have also demonstrated earlier that SSPD's operating in the HEMT readout configuration are able to distinguish photons of different energies.<sup>13</sup> Therefore, here we focus on the PNR capability of an SSPD connected directly to HEMT.

As stressed before, in the case of devices with  $I_c \approx 5 \mu\text{A}$  and the HEMT  $R_L = 500 \Omega$ , one should still be able to distinguish, at least qualitatively, between the single- and multiphoton events. Indeed, when the laser intensity and  $I_{\text{bias}}$  were increased so that the detector started to register nearly every incident light pulse while the dark counts were still low, one could observe that, in time-domain traces of the photoresponse counts, some pulses exhibited visibly higher amplitudes than the rest. Figure 129.53 shows an example of such a real-time trace, which although convincing, is absolutely insufficient to conclude that these large pulses were indeed caused by double-photon events, instead of, e.g., a single-photon event arriving close in time to a dark-count event, or even resulting from a large inhomogeneity of the meandering stripe. It was, therefore, again necessary to look at the statistics of the pulse-amplitude distributions. This time, both the intensity of laser pulses and  $I_{\text{bias}}$  were varied for each case, and amplitudes of several million pulses were collected. Ultraviolet photons (frequency-tripled Ti:sapphire beams) were used to increase the photon-detection efficiency of the SSPD.

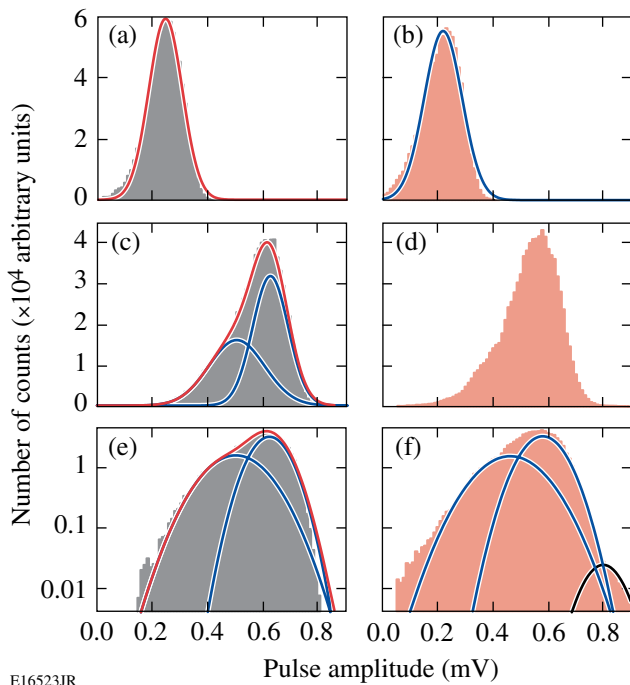
The results are presented in Fig. 129.54. When  $I_{\text{bias}} \approx 0.7 I_c$ , the amplitude distribution can be fit with a simple Gaussian function, as shown in Figs. 129.54(a) and 129.54(b). Once  $I_{\text{bias}}$  reached  $0.9 I_c$ , however [as shown in Figs. 129.54(c) and 129.54(d)], one could see a spreading of the distribution, which now had to be fit with two Gaussians. Although the two-Gaussian distribution can be explained as a result of



E16522JR

Figure 129.53

Live oscilloscope time-domain trace, showing higher amplitudes of some pulses.



E16523JR

Figure 129.54

Pulse-amplitude histograms for (a)  $n \ll 1$ ,  $I_{\text{bias}} = 0.7 I_c$ ; (b)  $n \leq 1$ ,  $I_{\text{bias}} = 0.7 I_c$ ; (c)  $n \ll 1$ ,  $I_{\text{bias}} = 0.9 I_c$ ; (d)  $n \leq 1$ ,  $I_{\text{bias}} = 0.9 I_c$ ; (e) semi-log plot of (c); and (f) semi-log plot of (d). Gray histograms indicate the same incident photon flux for the  $n \ll 1$  regime; red histograms indicate the same incident photon flux for the  $n \leq 1$  regime.

significant nonuniformity variations of the NbN stripe rather than the PNR phenomenon, a more-detailed analysis of the presented plots favors the PNR interpretation. Figures 129.54(e)

and 129.54(f) show the same data as Figs. 129.54(c) and 129.54(d), respectively; however, they are replotted on a semi-log scale. In Fig. 129.54(f) one can notice that, in the single-photon  $n \leq 1$  regime, there is actually a third small Gaussian peak. This peak, however, is completely absent in the  $n \ll 1$  regime [Fig. 129.54(e)], as well as when  $I_{\text{bias}}$  is far below  $I_c$  [Figs. 129.54(a) and 129.54(b)]. This third peak also cannot be a result of dark counts since the dark counts are most pronounced in the case of  $n \ll 1$  illumination, as demonstrated in Fig. 129.52. Taking into account that the mean amplitude of this third Gaussian peak is the largest, the most-reasonable, although tentative, explanation is that it is indeed a result of the SSPD detection of multiphoton events. Further analysis is needed, however, to either support or disprove this conclusion.

### Conclusion

In conclusion, we were able to observe the difference between dark counts and photon counts generated in our meander-type NbN SSPD's by utilizing an HEMT readout technique and, subsequently, examining distribution widths of the histograms of amplitudes of the collected in real-time dark- and photon-count signals. The distribution width for the dark count events was very narrow and independent of the bias current, while the FWHM of the distribution in the case of photon counts was up to  $4\times$  wider and was directly related to the photon flux (the average number of photons per pulse) incident on the SSPD. The differences in the measured FWHM values of the output-pulse distributions could be satisfactorily explained by the different physical origin of the dark-count events (VAP breaking and Lorentz-force dissipation) and the photon-count events (photon-induced hot-spot formation). It has also been demonstrated that the HEMT readout offers a promise of PNR functionality in SSPD measurements. The next step in this direction is likely to come from implementing ferromagnet/superconductor bilayer nanostripes (e.g., NiCu/NbN heterostructures), which are not only characterized by picosecond quasiparticle-phonon relaxation dynamics but also exhibit almost an order-of-magnitude larger superconductor critical-current densities.<sup>25</sup>

### ACKNOWLEDGMENT

The authors thank Prof. G. Gol'tsman and his group at the Moscow State Pedagogical University for their assistance in the sample preparation and Prof. H. Mooij for very helpful discussions. Research in Warsaw was supported by the Polish Ministry of Science under Project No.4426/B/TO2/2007/33. R. S. thanks the Spanish Ministry of Education and the University of Salamanca for their financial support and hospitality during his one-semester-long research visit in Salamanca, Spain.

REFERENCES

1. W. Słysz, M. Węgrzecki, J. Bar, P. Grabiec, M. Górška, V. Zwiller, C. Latta, P. Böhi, A. J. Pearlman, A. S. Cross, D. Pan, J. Kitaygorsky, I. Komissarov, A. Verevkin, I. Milostnaya, A. Korneev, O. Minaeva, G. Chulkova, K. Smirnov, B. Voronov, G. N. Gol'tsman, and R. Sobolewski, *J. Mod. Opt.* **54**, 315 (2007).
2. C. Bennett and G. Brassard, in *International Conference on Computers, Systems, and Signal Processing* (IEEE Computer Society, IEEE Circuits and Systems Society, and Indian Institute of Science, Bangalore, India, 1984), pp. 175–179.
3. E. Waks, A. Zeevi, and Y. Yamamoto, *Phys. Rev. A* **65**, 052310 (2002).
4. E. Knill, R. Laflamme, and G. J. Milburn, *Nature* **409**, 46 (2001).
5. E. Reiger, S. Dorenbos, V. Zwiller, A. Korneev, G. Chulkova, I. Milostnaya, O. Minaeva, G. Gol'tsman, J. Kitaygorsky, D. Pan, W. Słysz, A. Jukna, and R. Sobolewski, *IEEE J. Sel. Top. Quantum Electron.* **13**, 934 (2007).
6. Y. Kang *et al.*, *Appl. Phys. Lett.* **85**, 1668 (2004).
7. G. Ribordy *et al.*, *J. Mod. Opt.* **51**, 1381 (2004).
8. G. N. Gol'tsman, O. Okunev, G. Chulkova, A. Lipatov, A. Semenov, K. Smirnov, B. Voronov, A. Dzardanov, C. Williams, and R. Sobolewski, *Appl. Phys. Lett.* **79**, 705 (2001).
9. K. M. Rosfjord *et al.*, *Opt. Express* **14**, 527 (2006).
10. J. Kitaygorsky, J. Zhang, A. Verevkin, A. Sergeev, A. Korneev, V. Matvienko, P. Kouminov, K. Smirnov, B. Voronov, G. Gol'tsman, and R. Sobolewski, *IEEE Trans. Appl. Supercond.* **15**, 545 (2005).
11. A. Engel *et al.*, *Phys. Stat. Sol. C* **2**, 1668 (2005).
12. J. Kitaygorsky, I. Komissarov, A. Jukna, D. Pan, O. Minaeva, N. Kaurova, A. Divochiy, A. Korneev, M. Tarkhov, B. Voronov, I. Milostnaya, G. Gol'tsman, and R. Sobolewski, *IEEE Trans. Appl. Supercond.* **17**, 275 (2007).
13. J. Kitaygorsky, S. Dorenbos, E. Reiger, R. Schouten, V. Zwiller, and R. Sobolewski, *IEEE Trans. Appl. Supercond.* **19**, 346 (2009).
14. M. G. Bell *et al.*, *IEEE Trans. Appl. Supercond.* **17**, 289 (2007).
15. G. N. Gol'tsman, K. Smirnov, P. Kouminov, B. Voronov, N. Kaurova, V. Drakinsky, J. Zhang, A. Verevkin, and R. Sobolewski, *IEEE Trans. Appl. Supercond.* **13**, 192 (2003).
16. W. Słysz, M. Węgrzecki, J. Bar, P. Grabiec, M. Górška, V. Zwiller, C. Latta, P. Bohi, I. Milostnaya, O. Minaeva, A. Antipov, O. Okunev, A. Korneev, K. Smirnov, B. Voronov, N. Kaurova, G. Gol'tsman, A. Pearlman, A. Cross, I. Komissarov, A. Verevkin, and R. Sobolewski, *Appl. Phys. Lett.* **88**, 261113 (2006).
17. A. J. Kerman *et al.*, *Appl. Phys. Lett.* **88**, 111116 (2006).
18. J. K. W. Yang *et al.*, *IEEE Trans. Appl. Supercond.* **17**, 581 (2007).
19. A. VI. Gurevich and R. G. Mints, *Rev. Mod. Phys.* **59**, 941 (1987).
20. T. Taneda, G. P. Pepe, L. Parlato, A. A. Golubov, and R. Sobolewski, *Phys. Rev. B* **75**, 174507 (2007).
21. D. Pan, G. P. Pepe, V. Pagliarulo, C. De Lisio, L. Parlato, M. Khafizov, I. Komissarov, and R. Sobolewski, *Phys. Rev. B* **78**, 174503 (2008).
22. A. Pearlman, A. Cross, W. Słysz, J. Zhang, A. Verevkin, M. Currie, A. Korneev, P. Kouminov, K. Smirnov, B. Voronov, G. Gol'tsman, and R. Sobolewski, *IEEE Trans. Appl. Supercond.* **15**, 579 (2005).
23. J. E. Mooij, in *Percolation, Localization, and Superconductivity*, edited by A. M. Goldman and S. A. Wolf, NATO ASI, Series B, Vol. 109 (Plenum Press, New York, 1984), pp. 325–370.
24. A. M. Kadin, *J. Appl. Phys.* **68**, 5741 (1990).
25. N. Marrocco, G. P. Pepe, A. Capretti, L. Parlato, V. Pagliarulo, G. Peluso, A. Barone, R. Cristiano, M. Ejrnaes, A. Casaburi, N. Kashiwazaki, T. Taino, H. Myoren, and R. Sobolewski, *Appl. Phys. Lett.* **97**, 092504 (2010).